

New Insights into the Bulk and Surface Defect Structures of Ceria Nanocrystals from Neutron Scattering Study

Si Luo, Meijun Li, Victor Fung, Bobby G. Sumpter, Jue Liu,* Zili Wu,* and Katharine Page*



Cite This: *Chem. Mater.* 2021, 33, 3959–3970



Read Online

ACCESS |



Metrics & More

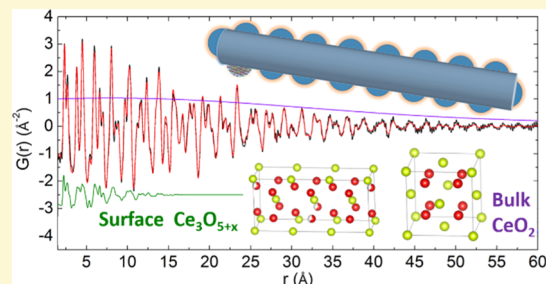


Article Recommendations



Supporting Information

ABSTRACT: Neutron diffraction and pair distribution function studies coupled with Raman spectroscopy have successfully unraveled the detailed oxygen defect structures of ceria nanocubes and nanorods. Two types of defect sites are revealed for the ceria nanocrystals: surface and bulk defects. It is proposed that the surface oxygen defects in both types of CeO_2 nanocrystals are predominantly the partially reduced $\text{Ce}_3\text{O}_{5+x}$ with the bulk defect structures dominated by interstitial Frenkel-type oxygen vacancies. Ceria nanorods possess much higher concentration of surface oxygen defects relative to the nanocubes, albeit with only slightly higher concentration of bulk Frenkel-type oxygen vacancies. Upon annealing the nanorod sample at 600 °C under vacuum ($\sim 10^{-4}$ to 10^{-5} mbar), a partially reduced ceria phase with long-range oxygen vacancy ordering ($\text{Ce}_3\text{O}_{5+x}$) has been observed experimentally for the first time. This intriguing observation that surface defect phases can take on ordered defect sublattices under certain conditions is of great value in understanding the temperature-dependent catalytic performance of ceria nanocrystals. Furthermore, a drastic decrease of the surface vacancies in the ceria nanocrystals is observed upon exposure to SO_2 , especially for the nanorods, a likely origin for the sulfur poisoning effect on ceria-based materials. This study suggests that tailoring surface morphology is a promising strategy to control defect properties of ceria nanomaterials. It also provides fundamental insights to stabilize surface oxygen defects in CeO_2 nanocrystals to achieve high redox performance under corrosive environments such as under SO_2/SO_x exposure.



1. INTRODUCTION

CeO_2 has been broadly used in the purification of exhaust gas in three-way catalysts for automotive pollution control.^{1–6} It has also been widely used as an electrolyte for solid oxide fuel cells and effective catalysis support for water gas shift reactions.^{4,6,7} In all these applications, the superior mobility of lattice oxygen and excellent redox properties associated with $\text{Ce}^{4+}/\text{Ce}^{3+}$ play critical roles. It is generally agreed that the excellent dynamic oxygen storage capacity (OSC) of ceria is strongly correlated with the presence of oxygen defects.^{8–10} It has been broadly reported that OSC can be drastically increased by creating large amounts of oxygen defects. This has inspired optimization strategies such as aliovalent cation doping/substituting to improve the performance of ceria.^{11–14} It has been proposed that the redox properties of ceria are controlled by the type, size, distribution, and location (surface or bulk) of the oxygen vacancies.^{8,10,13,15–17} Despite extensive investigations using a variety of characterization tools, such as spectroscopy (X-ray photoelectron spectroscopy and Raman spectroscopy), diffraction (X-ray and neutron), and scanning tunneling microscopy,^{10,13,15,17–21} the nature of oxygen vacancies in ceria is still fiercely debated. It has been previously observed that Ce maintains a valence state of 4+ in most oxidized CeO_2 samples with very limited amounts of Ce^{3+} .^{13,15} It has also been observed that the surface defects of ceria nanoparticles behave very differently compared to bulk

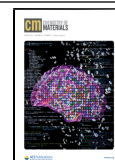
phases.^{15,22,23} Many researchers have reported the surface oxygen vacancy clustering on model ceria single crystals.^{8,17} Clustered defects on ceria surfaces or subsurfaces are believed to play key roles in the dynamic OSC performance and redox properties of ceria materials.^{8,24} It is worth noting that a majority of studies have been carried out using either CeO_2 single crystals with low energy (111) surface facets or polycrystalline ceria nanoparticles with mixed crystal surface terminations.^{10,17,21,25} However, many reports have highlighted that ceria crystals with selective exposed surface planes, such as {111}, {110}, and {100}, possess drastically different surface stability and vacancy ordering patterns relative to one another.^{10,26–29} Therefore, it is important and timely to investigate nanosized ceria with controlled terminations (facets) to better understand the facet-dependent defect sites and OSC performance of ceria.

The recent success of synthesizing ceria nanocrystals with well-controlled morphology, such as nanooctahedra, nano-

Received: January 15, 2021

Revised: May 14, 2021

Published: May 27, 2021



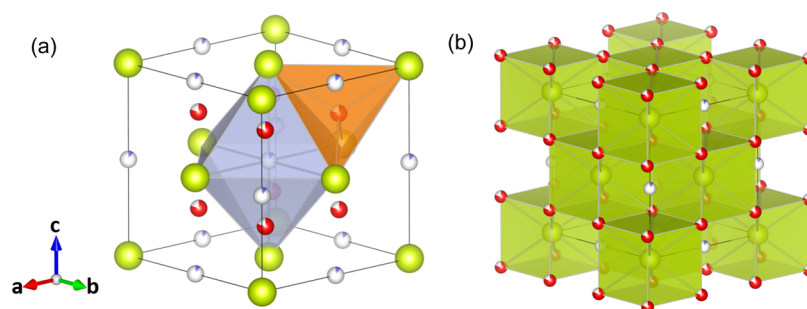


Figure 1. (a) Potential oxygen positions within the fluorite tetrahedral sites (orange-colored OCe_4) and interstitial octahedral sites (gray-colored OCe_6) in CeO_2 and (b) structure of CeO_2 shown with a CeO_8 (light green) polyhedron in the classic fluorite structure. Ce atoms are shown as light green spheres and O atoms are shown as white spheres that are shaded (red for tetrahedral and gray for octahedral) according to their respective partial occupancies.

cubes, and nanorods, has paved the way to investigate the facet-dependent properties of ceria.^{10,15,27,29–32} Particularly, ceria nanocubes and nanorods with high energy surface terminations have attracted tremendous attention in the past decade because of their excellent OSC and oxidation activities.^{8,15,26,27,33} Although it has been broadly acknowledged that this is strongly correlated with the concentration of defects, the nature of these defects in different faceted ceria nanocrystals is still not fully understood. For small nanoparticles, such as nanorods with a diameter of ~ 10 nm, the surface/subsurface (around 5 Å or two layers of Ce–O bonds) is over 20% of the total volume. Therefore, it is very likely that the concentration, types, and inter-relationships of surface/surface defects differ drastically from those found in bulk ceria. Such materials present a novel opportunity to understand the nature of both surface/subsurface and bulk oxygen defects in ceria nanocrystals.

Despite the excellent OSC and oxidative reactivity of ceria nanocrystals terminated with high energy surfaces, their application has been limited due to their relatively poor resistivity to toxic environments such as in automotive exhausts. Among the various catalytic poisoning mechanisms, SO_2 has been broadly reported to cause the deactivation of ceria.^{34–38} Despite extensive investigations, the detailed mechanism regarding the SO_2 poisoning is still fiercely debated, especially for ceria nanocrystals with high energy surfaces. Thus, it is of great importance to quantify the nature and modification of the structure, especially the defect structure, that ceria nanocrystals (with different exposed facets) experience upon SO_2 exposure.

In this work, valuable details about oxygen defects (both surface and bulk) of fresh and sulfated ceria nanorods and nanocubes were obtained by quantitative structure refinement using temperature-dependent neutron total scattering data, which is highly sensitive to local structural environments of light elements such as oxygen, in combination with UV resonance Raman spectroscopy characterization. Particularly, we present the first experimental observation of an oxygen vacancy-ordered phase ($\text{Ce}_3\text{O}_{5+x}$) on the surface of ceria nanorods, underscoring the need to better understand the evolution of surface defects on high energy facets. Furthermore, the evolution of both surface/subsurface and bulk oxygen vacancies upon SO_2 treatment has been successfully unraveled. Our results demonstrate that SO_2 treatment drastically decreases the amount of surface oxygen vacancies at elevated temperatures. This could effectively block the oxygen vacancy exchange between the surface and the bulk

of ceria nanocrystals. It also highlights that the stability of surface oxygen defects is critical in the OSC and catalytic performance of ceria nanoparticles.

2. EXPERIMENTAL SECTION

2.1. Pre-reduced and Sulfated CeO_2 Preparation. CeO_2 nanorods and nanocubes were prepared as described in ref 24.²⁴ Each CeO_2 sample was loaded into a U tube and then oxidized at 400 °C for 1 h by 5% O_2/Ar . After He purging at 400 °C, 4% H_2/Ar was introduced for 2 h to reduce the sample. The sample was cooled down to 300 °C in He to remove H_2 , and then 2% SO_2/He was introduced into the reactor and held at 300 °C for 2 h. Controlled experiments were conducted on CeO_2 that was treated with O_2 and then H_2 exactly as described for the sulfated sample but without SO_2 exposure.

2.2. OSC Measurements. About 30 mg of the sample was loaded into a quartz U tube in an AMI 300 chemisorption analyzer. After pretreatment in O_2 at 400 °C for 1 h, the sample was reduced at 400 °C in H_2 for 2 h. After 40 min of He purging, pulses of 5% O_2 were injected into the sample with He as the carrier gas. One pulsing takes 1 min, followed by 2 min of refilling of the 0.5 mL loop. Ten pulses were monitored by a quadruple mass spectrometer (OmniStar GSD 320), and then five calibration pulses were injected with the same condition but bypassing the U tube reactor.

2.3. Raman Spectroscopy. The Raman spectra of the pre-reduced ceria and the SO_2 -treated ceria samples were recorded at ambient condition with a 325 nm laser excitation (<5 mW at sample) from a HeCd laser (Melles Griot). Raman scattering was performed via a customized ellipsoidal mirror and directed by a fiber optics bundle to the spectrograph stage of a triple Raman spectrometer (Princeton Instruments Acton Trivista 555). An edge filter (Semrock) was used in front of the UV–vis fiber optic bundle (Princeton Instruments) to block the laser irradiation. A UV-enhanced liquid N_2 -cooled CCD detector (Princeton Instruments) was employed for signal detection.

2.4. Neutron Total Scattering Data Collection. Neutron diffraction and pair distribution function (PDF) data were collected at the NOMAD beamline at the Spallation Neutron Source, Oak Ridge National Laboratory. NOMAD is a high-flux, medium-resolution powder diffractometer dedicated to neutron total scattering and PDF studies. The very high-flux and large detector coverage enables fast data collection using small amounts of samples (e.g., hundreds of milligrams), which is crucial for studying nanocatalysts. For the current experiment, about 0.3–0.5 g of CeO_2 nanoparticles were loaded into a 6 mm vanadium can and into the vacuum furnace (ILL) for temperature-dependent studies. The vacuum was maintained at a pressure lower than 10^{-4} to 10^{-5} mbar during the entire heating and cooling process. Four 30 min scans were collected at each temperature point and then summed together to improve the statistics of the data. Signal from the empty vanadium can measurements was subtracted as background from the sample measurement and data were normalized by the scattering intensity from a 6 mm vanadium rod to correct for detector efficiencies. No

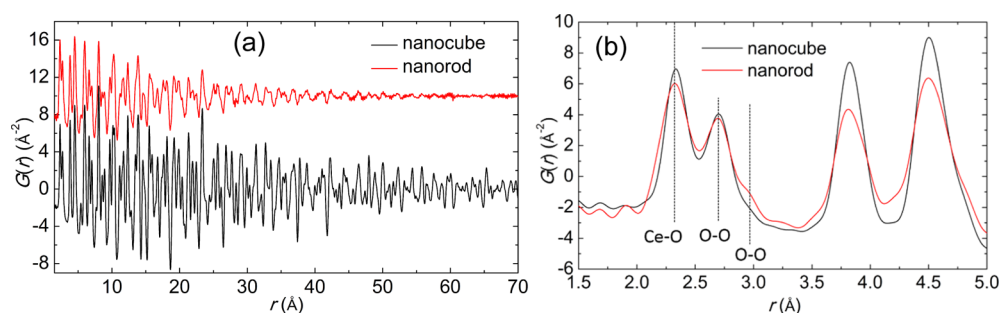


Figure 2. Neutron PDF of pre-reduced CeO_2 nanocube and nanorod, with the comparison of long-range PDF (1.5–70.0 Å, offset for comparison of the long-range intensities) shown on the left (a) and the local PDF (1.5–5.0 Å, with the two patterns overlaid for comparison) on the right (b).

absorption correction was applied due to the very small absorption cross section associated with Ce and O.

2.5. Density Function Theory Calculations. Formation energies of Ce_3O_5 bulk structures with various oxygen vacancy arrangements were calculated. Density functional theory (DFT) calculations were performed with the Vienna Ab Initio Simulation Package.^{39,40} The Perdew–Burke–Ernzerhof⁴¹ functional within the generalized gradient approximation was used for the electron exchange and correlation. The projector-augmented wave method was used to describe the electron-core interaction.^{39,42} A kinetic energy cutoff of 450 eV was used. All calculations were performed with spin polarization. The on-site Coulomb interaction was included with the DFT + U method by Dudarev et al.⁴³ using a Hubbard parameter $U = 5$ eV based on previous studies for CeO_2 .³⁷ The Brillouin zone was sampled using a Monkhorst–Pack scheme.⁴⁴

2.6. Structure Models and Refinements. Ceria crystallizes in the conventional fluorite structure with the space group of $Fm\bar{3}m$, wherein every Ce^{4+} is surrounded by eight O^{2-} , forming a CeO_8 cube, as can be seen in Figures 1 and S1. Every O^{2-} is bonded to four Ce^{4+} , forming an OCe_4 tetrahedron. The interstitial octahedral site formed by six Ce is vacant and allows the formation of potential Frenkel-type oxygen defects, that is, with oxygen partially moving from the original OCe_4 tetrahedral site to the interstitial OCe_6 octahedral site.²¹ According to previous reports, there is also the possibility that oxygen on the original tetrahedral site displaces along the $\langle 110 \rangle$ and $\langle 111 \rangle$ directions, forming partially degenerate sites.²¹ The original oxygen site has the degeneracy of 8, the interstitial octahedral site has the degeneracy of 24 (with site splitting), the split tetrahedral oxygen site along the $\langle 111 \rangle$ direction has a degeneracy of 32, and the split site along the $\langle 110 \rangle$ direction has a degeneracy of 96. In this study, we found that splitting of the oxygen tetrahedral site is very limited when refined against the short- to intermediate-range neutron PDF data. Therefore, only the original oxygen tetrahedral site and the interstitial octahedral site (with site splitting and a degeneracy of 24) were incorporated into the bulk-phase model. This defect fluorite structure model is typically denoted as CeO_{2-x} . In addition to this defect fluorite main phase, our investigation revealed the presence of a partially reduced surface structure ($\text{Ce}_3\text{O}_{5+x}$), whose details will be discussed in the Results and Discussion section.

Structure refinements were carried out using TOPAS v6 software.⁴⁵ For the Bragg diffraction data analysis, time-of-flight (TOF) data were converted to d -spacing data using the conventional second-order polynomial $\text{TOF} = \text{ZERO} + \text{DIFC} \times d + \text{DIFA} \times d^2$, where ZERO is a constant, DIFC is the diffractometer constant, and DIFA is an empirical term to correct for sample displacement and absorption-caused peak shift. ZERO and DIFC were determined from refinement of a standard NIST Si-640e data set and held fixed, while DIFA was allowed to vary during refinements to account for sample displacement. A back-to-back exponential function convoluted with a symmetrical Gaussian function was used to describe the peak profile. For PDF data analysis, the instrument constants Q_{broad} and Q_{damp} were determined from the refinement of a Si-640e standard to be 0.19 and 0.21 \AA^{-1} , separately. A numerical approach was used to quantify the shape and size effect for the CeO_2 nanorods; more details about this

method can be found in related references.⁴⁶ Isotropic atomic displacement parameters were used for both Bragg diffraction and PDF data-based structure refinements.

3. RESULTS AND DISCUSSION

3.1. Structure, Morphology, and the Nature of Oxygen Vacancies in CeO_2 Nanorods and Nanocubes.

Pre-reduced CeO_2 nanocube and nanorod samples were used as model systems for the current investigation. Neutron PDF data of the two samples are shown in Figure 2a. It can be seen that strong $G(r)$ peaks extend to large atomic pair distances for the nanocube sample (black curve in Figure 2a), while the $G(r)$ signal diminishes significantly at approximately 60 Å for the nanorod sample. Considering the rod shape,^{15,24} this indicates that the coherent length across the diameter of nanorods is less than 60 Å. A careful examination of the PDF (Figure 2b) reveals important atomic structural distinctions in the CeO_2 nanorods relative to the nanocubes. The first $G(r)$ peak at approximately 2.4 Å is solely from the nearest Ce–O pair, with the nanorod sample showing a much broader nearest Ce–O correlation with slightly asymmetric tail toward the low r direction. Similar features are observed for the peaks around 3.7 and 4.6 Å but with the asymmetric peak tails extending toward the opposite (high r) direction. The second pair–pair correlations in ceria correspond to the nearest O–O pair distances in the ideal fluorite CeO_2 structure, around 2.73 Å (Figure S1). A peak shoulder is apparent at 2.9 Å and is much stronger in the nanorod data relative to the nanocube data. This shoulder peak is very likely associated with the much longer distanced O–O pair in the reduced CeO_{2-x} phases. In all, these qualitative observations indicate that the short-range structure of pre-reduced CeO_2 nanorods differs drastically from that of the nanocubes.

The bulk oxygen defects in CeO_2 nanoparticles have been extensively investigated using a variety of diffraction and spectroscopy characterization tools.^{13,15,21} It is now generally agreed that the bulk oxygen defects are predominantly Frenkel-type defects; that is, oxygen partially occupies the interstitial octahedral sites (OCe_6) while the original tetrahedral sites (OCe_4) are partially vacant in the classic fluorite structure, as can be seen in Figure 1. This classic defect model was further confirmed by a recent Reverse Monte-Carlo analysis.⁴⁷ In contrast, the surface oxygen defects, especially those formed on the high energy surfaces, for example, $\{110\}$ or $\{100\}$, of small nanoparticles are still not well understood. Accordingly, we started our quantitative structure refinements of the nanocube and nanorod samples with the proposed classic Frenkel-type defects. Structure refinements of the CeO_2 nanocube using neutron Bragg diffraction data and intermediate-range neutron

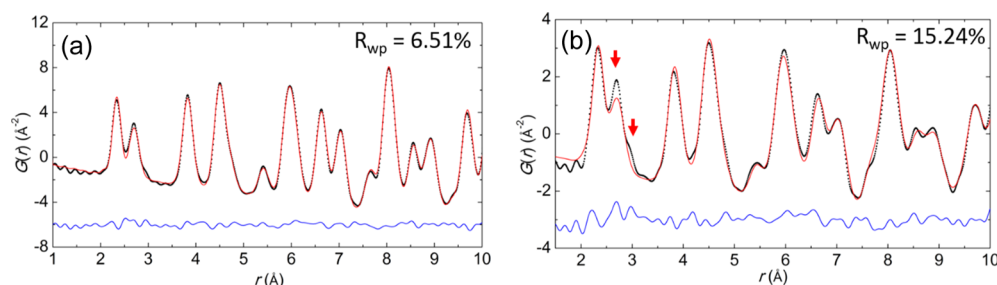


Figure 3. Structure refinements of CeO₂ nanocubes (a) and nanorods (b) using short-range neutron PDF data (1.5–10 Å). The classic Frenkel-type defects were implemented during the refinements. The red arrows highlight the regions with large discrepancies.

PDF data (10–30 Å) suggest very limited amounts of both Ce³⁺-induced oxygen defects (V_{O}) and Frenkel-type defects in the bulk structure (Figure S2). This suggests that Ce is predominantly 4+ in the nanocube, and there are very limited amounts of ordered Frenkel-type oxygen defects in the bulk structure of the CeO₂ nanocube. However, the local structure refinements using the short-range neutron PDF data (1.5–10 Å) clearly indicate the presence of Frenkel-type oxygen defects, and the defect concentration was refined to be 0.031(3) (~3%). To further confirm the reliability of the refinement, we have tested the refinement quality (residual values) as a function of the concentration of the Frenkel-type defects (Figure S3). Indeed, the result confirms that the current refinement is very sensitive to the oxygen Frenkel defects. The final refinement results can be found in Figure 3a and Table S1. It is worth noting that there is a slight discrepancy between the calculated result and the experiment data around the Ce–O and O–O nearest neighbor distances at 2.6 and 2.8 Å, with the presence of a very weak shoulder peak in the data that is not modeled using the ideal fluorite structure with Frenkel-type oxygen defects. This indicates that the short-range atomic environments differ from the average structure picture obtained from Bragg diffraction data, even for the large-sized nanocubes.

A similar structure refinement strategy was adopted for the nanorod sample. It is worth noting that there is an appreciable hydrogen signal in the neutron diffraction pattern (Figure S4), which is very likely due to a hydroxyl (–OH)-terminated surface. The concentration of Frenkel-type defects is refined to be 0.021(2) using neutron Bragg diffraction data and it is refined to be 0.062(7) when using short-range neutron PDF data (1.5–10 Å), indicating that the nanorod sample possesses slightly higher concentration of bulk Frenkel-type oxygen vacancies relative to that of the nanocube sample at room temperature. In addition, more dramatic discrepancy can be seen in the Ce–O and O–O pair distances at 2.6 and 2.8 Å in the nanorod sample, and the shoulder peak around 2.9 Å is also much stronger relative to the nanocube sample (Figures 2b and 3b). Taken together, this drastic difference between the nanocube and nanorod is very likely caused by the difference in the nature or amount of the corresponding surface/subsurface defect (the nanorod has much smaller size and thus a significantly higher surface-to-volume ratio than the nanocube).²⁴ In addition, the bulk structure refinements of both samples using intermediate range PDF data (10–30 Å) do not exhibit obvious discrepancies from the features of the fluorite bulk structure with Frenkel-type defects, suggesting that the observed discrepancies at local atomic pair distances are very likely located on the surface/subsurface of ceria nanocrystals.

To quantitatively refine the surface and bulk structure of ceria nanocubes and nanorods, we employed a two-phase model, a bulk structure with Frenkel-type defects combined with a surface oxygen defect structure phase. Since nanorods possess much higher surface/subsurface areas (estimated to be over 20% of the total volume) relative to the nanocubes (estimated to be less than 5% of the total volume) based on the particle size,²⁴ local structure modeling was first completed on the ceria nanorod data. It is worth noting that detailed morphology information is absent from the experimental PDF [$G(r)$] data due to the lack of low- Q scattering data at dedicated PDF instruments ($Q_{\text{min}} \approx 0.1 \text{ \AA}^{-1}$ or higher). The influence of particle shape nonetheless manifests as a dampened high- r PDF signal at dimensions approaching the correlation length scale(s) intrinsic to the particle's atomic structure. This effect can be modeled in small box modeling by implementing a characteristic shape function $\gamma_0(r)$, or the so-called envelope function, into the PDF analysis process.^{48–50} For the current modeling, it is assumed that the surface-defected ceria phases are very small nanoparticles (~1 nm or less) decorating the bulk ceria nanorod (Figure 5b), a model that has been previously suggested in transmission electron microscopy (TEM) studies.²⁴ The analytic characteristic shape function of spherical particles ($1 - 1.5 r/d + 0.5 (r/d)^2$), where d is the diameter of the particle, was used to correct for the shape-/size-induced dampening of PDF data of the surface defect phase, and a numerical double Gaussian function was adopted to approximate the shape correction for the nanorod.^{46,51} In order to refine the dimensions of the nanorod, a large range (1.5–60 Å) of neutron PDF data was used for the structure refinement.

As mentioned in the previous section, the presence of the 2.9 Å shoulder peak indicates the existence of two distinct nearest O–O pair distances in the structure (the original nearest O–O pair distance is around 2.73 Å in the fluorite CeO₂). Moreover, the Ce–O bond distance disproportionation (around 2.4 and 2.6 Å) indicates that appreciable amounts of reduced Ce³⁺ exist in the defect structure. However, the reduced phase is unlikely to be the fully reduced Ce₂O₃, as this phase possesses much longer average Ce–O bond distances and it also does not possess the O–O pair distances at 2.9 Å. Thus, these features are very likely associated with a surface defect phase. A variety of partially reduced ceria phases with oxygen vacancy ordering, such as Ce₁₁O₂₀ (1/11 oxygen vacancy), Ce₇O₁₂ (1/7 oxygen vacancy), and Ce₃O₅ (1/6 oxygen vacancy), have been previously observed or theoretically predicted either in the bulk phase or on the (111) surface.^{52–54} However, very limited reports can be found regarding defect structures on the high energy ceria surface (e.g., {110} or {100} facets), largely due to the lack of large

single crystals with high energy surfaces (for scanning TEM or other microscopy studies) and the difficulty of studying surface defect structures of ceria nanocrystals using conventional Bragg diffraction techniques.

The potential oxygen vacancy ordering patterns on the $\{110\}$, $\{100\}$, and $\{111\}$ facets are shown in Figures 4 and S6.

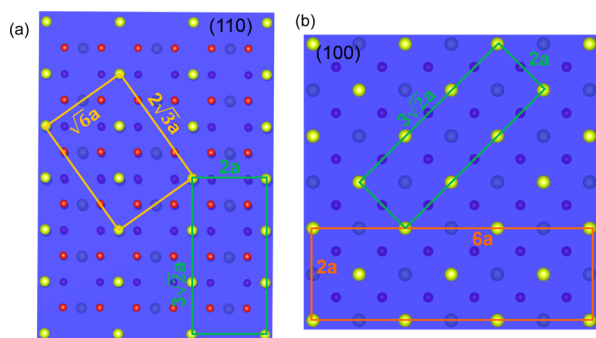


Figure 4. Potential oxygen vacancy (5:1) ordering patterns for the partially reduced ceria on the (110) (a) and (100) (b) surface of ceria nanocrystals. If one oxygen within the two-dimensional superlattice is fully vacant, then the 1/6 ordering pattern represents a composition of Ce_3O_5 (1/6 oxygen vacancy). It is also worth noting that the nanocube is predominantly terminated with $\{100\}$ facets while the nanorod has been reported to terminate with either $\{110\}$ or $\{100\}$ facets. Note: here, a represents the shortest O–O distance in the fluorite CeO_2 . Ce and O are shown in yellow and red, respectively.

It can be seen that 1/11 ($\text{Ce}_{11}\text{O}_{20}$), 1/7 (Ce_7O_{12}), 1/6 (Ce_3O_5), and 1/4 ($\text{C}-\text{Ce}_2\text{O}_3$) type ordering can be identified on the $\{111\}$ surface. However, only 1/6 (Ce_3O_5) type oxygen vacancy ordering patterns can be identified on the $\{110\}$ and $\{100\}$ surface. It is worth noting that the actual oxygen defect patterns on high energy ceria surfaces are likely to be a complex mixture of multiple ordering domains, similar to those observed on the $\{111\}$ surface.^{17,55} Here, $\text{Ce}_3\text{O}_{5+x}$ ($0 < x < 1$) with 1/6 oxygen vacancy ordering is chosen as the model surface defect structure for the nanocube and nanorod. Since there is still argument regarding the surface termination for ceria nanorods, both $\text{Ce}_3\text{O}_{5+x}$ structures on $\{110\}$ and $\{100\}$ were tested as the potential surface defect structures. The space group for the superstructure on $\{110\}$ facets with a $3\sqrt{2}a$ by $2a$ by $\sqrt{2}a$ (here, a represents the shortest O–O distance in the fluorite CeO_2) supercell is $Pnn2$ and the corresponding

space group is $P31m$ with a $6a$ by $6a$ by $32a$ supercell, as can be seen in Figures 4a and S7a,b. The plausible space groups for the ones ordered on the $\{100\}$ facets are $Pnn2$ and $Pcmm$ (Figures 4b and S7c,d).

It turns out that the $Pnn2$ -ordered $\text{Ce}_3\text{O}_{5+x}$ better describes the observed local structure features, as can be seen in Figures 5a and S8–S10, for both ceria nanorods and nanocubes. It is generally accepted that oxygen vacancy order in stable bulk structures avoids certain relative positions such as $\langle 1/2, 0, 0 \rangle_F$, $\langle 1, 0, 0 \rangle_F$, and $\langle 3/2, 0, 0 \rangle_F$ corresponding to the first, fourth, and ninth neighbors in the oxygen sublattice. We adopted this rule to estimate the relative stability of the proposed oxygen-deficient Ce_3O_5 bulk structure. It can be seen that oxygen vacancies follow $\langle 1, 1, 2 \rangle_a$ and $\langle 1, 1, 0 \rangle_a$ arrangements ($\langle 1/2, 1/2, 1 \rangle_F$ and $\langle 1/2, 1/2, 0 \rangle_F$ in the notation of ref 53) in the $Pnn2$ structure (Figure S7b). If the cell is expanded along the c -axis, the $\langle 2, 0, 0 \rangle_a$ type of oxygen vacancy ordering emerges. However, since the oxygen vacancy site is only partially vacant, it is expected that the actual oxygen vacancy order along the c -axis follows $\langle 4, 0, 0 \rangle_a$ ($\text{C}-\text{Ce}_2\text{O}_3$ possesses this type of oxygen vacancy arrangements).⁵³ In the $P31m$ -type Ce_3O_5 bulk structure, the proposed oxygen vacancies are following the $\langle 1, 1, 0 \rangle_a$ ordering pattern (Figure S7a), which effectively avoids the energetically unfavorable $\langle 1, 0, 0 \rangle$, $\langle 2, 0, 0 \rangle$ and $\langle 3, 0, 0 \rangle$ positions. This is likely the energetically most favorable bulk Ce_3O_5 structure. For the $Pcmm$ superstructure derived from a (100) surface, large amounts of oxygen vacancies follow the $\langle 2, 0, 0 \rangle_a$ and $\langle 3, 0, 0 \rangle_a$ arrangements, which is likely the energetically least favorable. This has been further confirmed by the calculated formation energy of three different bulk structures using DFT (results in Figure S7e). Although the bulk Ce_3O_5 with S.G. $P31m$ has the lowest formation energy, we found that this structure provides a worse fit for both local and intermediate-range neutron PDF data relative to the $Pnn2$ phase for the nanorod sample, as can be seen in Figure S8. This is also consistent with the findings of a reconstructed bulk phase, which will be discussed in detail in the later section. Similarly, it is found that the $Pnn2$ phase provides a much better fit (relative to the $Pcmm$ phase) for the neutron PDF data for the nanocube sample (Figures S9 and S10). Thus, the $Pnn2$ $\text{Ce}_3\text{O}_{5+x}$ phase is adopted to describe the surface oxygen defect phase for both samples.

Incorporating this phase into the refinement improves the fit quality drastically (R_{wp} drops from 15.9 to 13.2%). The improvement of the fit quality is even more dramatic when

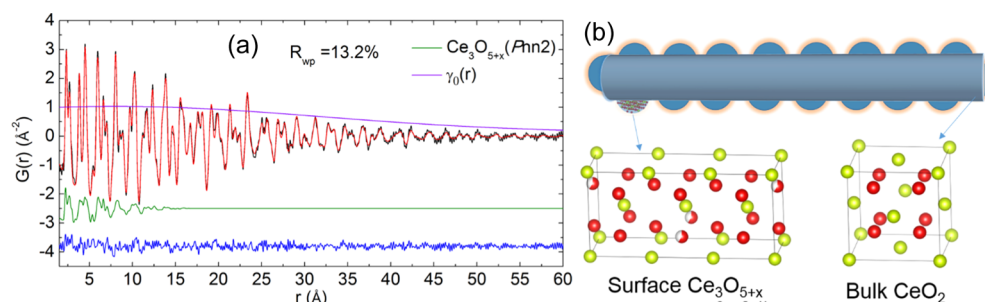


Figure 5. (a) Two-phase modeling of ceria nanorods (CeO_2 with Frenkel-type defects and $Pnn2$ -type $\text{Ce}_3\text{O}_{5+x}$) with the numerical nanorod shape correction. The contribution from surface $\text{Ce}_3\text{O}_{5+x}$ is highlighted in olive (shifted for clarification). The experimental data is shown in black, calculated curve in red, and difference curve in blue. The numerical approximation of the envelope function of the nanorod shape [$\gamma_0(r)$] is shown in purple. (b) Schematic illustration of the small spherical $\text{Ce}_3\text{O}_{5+x}$ nanoparticles decorating the surface of ceria nanorods (assuming that there is no interatomic interaction between these two phases). Crystal structures of the bulk fluorite CeO_2 phase and the surface defect $\text{Ce}_3\text{O}_{5+x}$ phase are shown at the bottom.

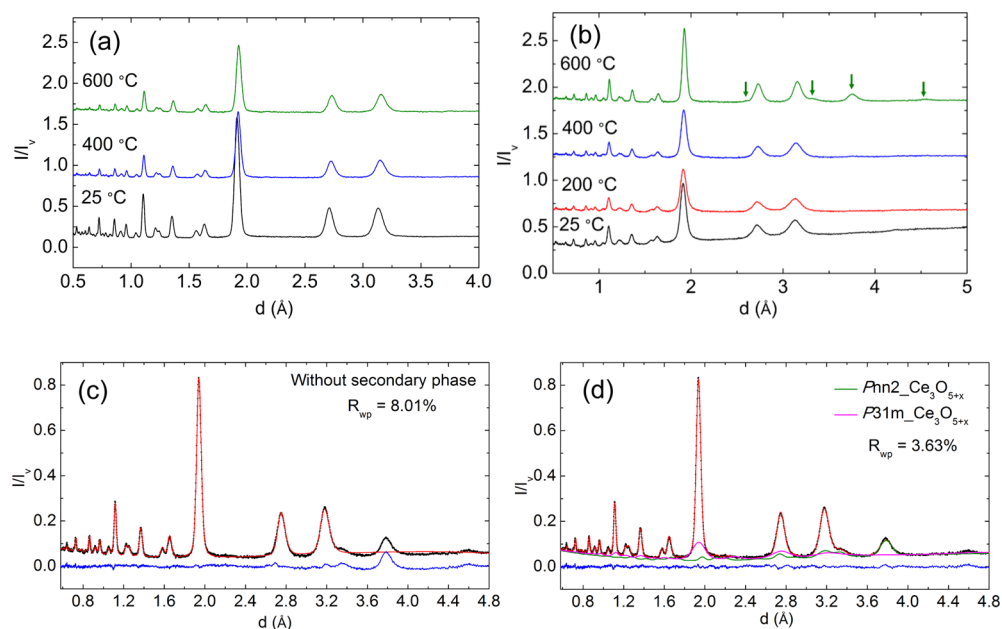


Figure 6. Neutron diffraction data (center $2\theta = 31^\circ$ bank) of ceria nanocube (a) and nanorod (b) as a function of experimental temperature. The olive colored arrows highlight the additional Bragg diffraction peaks appearing when the nanorod sample was annealed at 600 °C under vacuum (10^{-4} to 10^{-5} mbar). Structure refinement using neutron Bragg diffraction data of the ceria nanorod annealed at 600 °C using (c) ceria fluorite (single phase) and (d) combined fluorite CeO_2 and partially reduced $\text{Ce}_3\text{O}_{5+x}$ phases with two plausible space groups ($P2nn$ and $P31m$, highlighted in green and magenta separately).

using short-range neutron PDF data (1.5–10 Å), with the R_{wp} decreasing from 15.3% to 8.9%. The shoulder peak at around 2.9 Å can be well modeled after incorporating this surface defect phase. It can also be seen that this surface phase only contributes to about 15 Å, indicating that there is a very limited coherence length of this surface defect ceria phase. Although the incorporation of this surface defect phase drastically improves the fit, there is still noticeable discrepancy between the observed data and calculated data for the nearest O–O pair (around 2.73 Å, Figure S8a). This is very likely due to the interfacial bonding between the two phases or surface termination effects, that is, the particle surface is terminated with oxygen (or –OH) instead of Ce or O. A similar strategy was adopted for the analysis of the neutron PDF of the nanocube but with the supercell on the {100} surface (S.G. $Pnn2$). The refinement result can be found in Figures S9 and S10 and Tables S5–S12.

This defect model has been further confirmed by the UV Raman results (Figure S11). UV Raman has been recently proven to be very sensitive in characterizing different types of defects in ceria nanocrystals and aliovalent cation-doped ceria.^{15,18,56} It can be seen that the peak widths are much wider for the ceria nanorods relative to those of the nanocubes (Figure S11). This can be ascribed to the much smaller particle size and the stronger inhomogeneous strain (due to the larger amounts of defects) associated with ceria nanoparticles.⁵⁷ This result is fully consistent with our neutron scattering analysis. Furthermore, it is worth noting that the band at 597 cm^{-1} , which has been previously proposed to be caused by the defect-induced mode, is much broader than the peak associated with the F_{2g} mode of ceria (around 462 cm^{-1}), as can be seen in Figure S11.¹⁵ This indicates that the coherence length associated with the defects is much smaller relative to the size (coherence length) of the ceria nanocrystals, another conclusion in good agreement with the neutron PDF analysis.

To further understand the difference between the oxygen transport capability of ceria nanorod and nanocube, temperature-dependent neutron PDF data were collected at elevated temperatures (200, 400, and 600 °C for nanorods; 400 and 600 °C for nanocube) under vacuum condition. It was found that ceria nanorods grow dramatically after heating to 600 °C, as can be seen from the much sharper Bragg diffraction peaks (Figure 6b) and much decreased dampening of the high- r $G(r)$ signals (Figure S12b). Additional diffraction peaks to those parent fluorite phases can also be seen for the nanorod sample when heating to 600 °C (Figure 6b). In contrast, these extra diffraction peaks are not present in the nanocube sample when heating to 600 °C (Figure 6a), indicating that the formation of these phases is very likely dependent on the surface facet. Surface defect formation and reconstruction of CeO_2 under vacuum have attracted tremendous attention in the past decades, and a variety of reduced defect phases, such as $\text{Ce}_{11}\text{O}_{20}$, Ce_7O_{12} , and A or C-type Ce_2O_3 , have been observed.⁵³ More recently, a $(\sqrt{7}a \times 3a)$ R19.1° ordered supercell on the stable {111} facet has been observed under ultrahigh vacuum (10^{-8} mbar) at 1020 K.⁵⁴ We have thus tested all these potential reduced phases and found that none of them match the observed additional diffraction peaks. Instead, it is found that these peaks can be well indexed using a mixture of $3\sqrt{2}a$ by $2a$ by $\sqrt{2}a$ (S.G. $Pnn2$) and $3a$ by $2a$ by $2a$ (S.G. $Pcmm$) configurations (Figure S7), or the combination of $3\sqrt{2}a$ by $2a$ by $\sqrt{2}a$ (S.G. $Pnn2$) and $\sqrt{6}a$ by $\sqrt{6}a$ by $3\sqrt{2}a$ (S.G. $P31m$) (Figure S7). However, since the one with $3a$ by $2a$ by $2a$ superstructure (S.G. $Pcmm$) is energetically unfavorable (Figure S7e), the latter configuration (a combination of S.G. $Pnn2$ and $P31m$) is chosen for the final fit, as can be seen in Figures 6d and S13. This is exactly the proposed short-range oxygen vacancy-ordered superlattice ($\text{Ce}_3\text{O}_{5+x}$ with S.G. $Pnn2$ and $P31m$) on the {110} or {100} facets. This observation further confirms that the oxygen

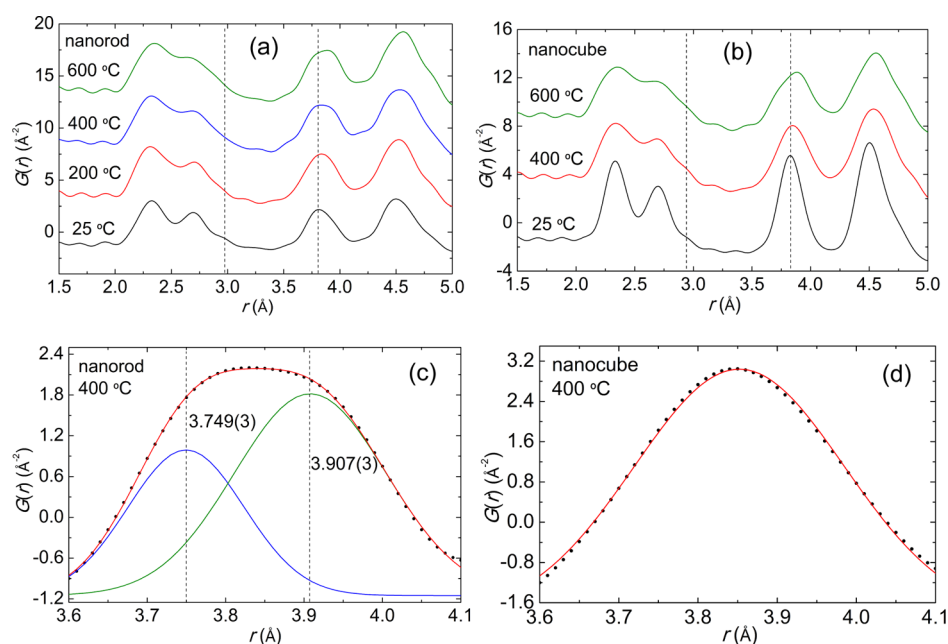


Figure 7. (a) Short-range neutron PDF data of pre-reduced CeO_2 nanorod (a) and nanocube (b) collected at different temperatures in a vacuum furnace ($<10^{-5}$ mbar). The peak splits around 3.8 Å for the nanorod sample (c) at 400 °C while this peak can be well modeled using a symmetrical Gaussian function for the nanocube sample (d) at the same temperature.

defects on the nanorod surface are not randomly distributed. Although it is currently difficult to quantitatively refine this defect structure due to the very broad nature of these diffraction peaks, it is very likely associated with the partially reduced $\text{Ce}_3\text{O}_{5+x}$ phases, emerging from the surface-defected phases during the particle growth and surface reconstruction of the nanorod above 400 °C under slightly reducing condition (vacuum). Further efforts are required to quantify these interesting new surface defect phases. These observations highlight that the defect formation on the high energy {110} facets differs from those on the low energy {111} facets, and it also confirms that there are relative larger amounts of surface oxygen defect phase in the nanorod sample relative to the nanocube sample upon reduction, as no superlattice peaks have been observed for the nanocube sample after heating to 600 °C (Figure 6a). This is in general agreement with previous Raman study and H_2 -TPR investigations that ceria nanorods are more reducible than nanocubes.^{15,58}

In order to study the shape and facet effect on the oxygen transport in the nanoparticles, we focus on data collected below/at 400 °C, where the facets of the ceria nanorods and nanocubes are well maintained. It can be seen that $G(r)$ around 3.8 Å forms two distinct peaks with a peak center position difference of about 0.15 Å at 400 °C (Figure 7). It is worth noting that this peak corresponds to the nearest Ce–Ce and the second nearest O–O distances in the ideal fluorite structure (Figure S1). Considering that the symmetry of the average structure is maintained, as can be seen from the Bragg diffraction data shown in Figure 6, this peak splitting indicates either the dispersion of local distribution of Ce and O or/and the partial formation of the oxygen-deficient phases. In contrast, this peak can be well described using a single Gaussian peak for the nanocube sample at 400 °C, though the splitting can be observed for the nanocube sample when heating up to 600 °C. Since the nearest Ce^{4+} – Ce^{4+} and the next nearest O–O distances are around 3.86 Å in the pristine nanocube and nanorod sample, it is expected that this value

will increase (instead of decrease) at higher temperature due to thermal expansion. The obvious decrease of this distance at higher temperature is very likely associated with the partially reduced Ce^{3+} (either on the surface/subsurface or bulk). The presence of Ce^{3+} in the lattice causes the local distortion of the lattice, such as the symmetrical distortion of the cerium and oxygen sublattices, as demonstrated in Figures 4, S6 and S7. This distortion with effectively decreased distances between potential reduced Ce^{3+} sites or between the oxygen vacancy sites is expected to lower the energy of the system. Peak fitting of this split peak using two Gaussian peaks can be found in Figure 7c. The intensity ratio between the lower r peak centered around 3.73–3.75 Å and the higher r peak around 3.9 Å decreases when heating to 600 °C. The decrease of this ratio indicates that the growth of particle size (as of 600 °C) decreases the amounts of the defect phases associated with Ce^{3+} , supporting the assumption that oxygen-deficient phase/phases are more likely present on the surface/subsurface of the nanocrystal. This assessment has been further confirmed by the observation in the nanocube sample, where this peak is well maintained as symmetric up to 400 °C, and the peak split emerges at 600 °C but with much weaker intensity for the lower r peak at about 3.7 Å.

Moreover, it is also worth noting that the shoulder peak around 2.95 Å smears into the very broad peak associated with the nearest O–O distance (centered at about 2.7 Å), indicating the increase in thermal vibration and the increase of the potential hopping between the nearest O–O sites. In contrast, this peak is well maintained in the nanocube when heated to 400 °C (Figure 7b), indicating that the hopping between the neighboring oxygen sites is lowered in the nanocube. In all, this temperature-dependent neutron PDF investigation indicates that there are larger amounts of Ce^{3+} containing oxygen-deficient phases in the nanorod sample relative to the nanocube sample at temperatures lower than 400 °C. Although heating up to higher temperature in general promotes the formation of these oxygen-deficient phases, as evidenced by the

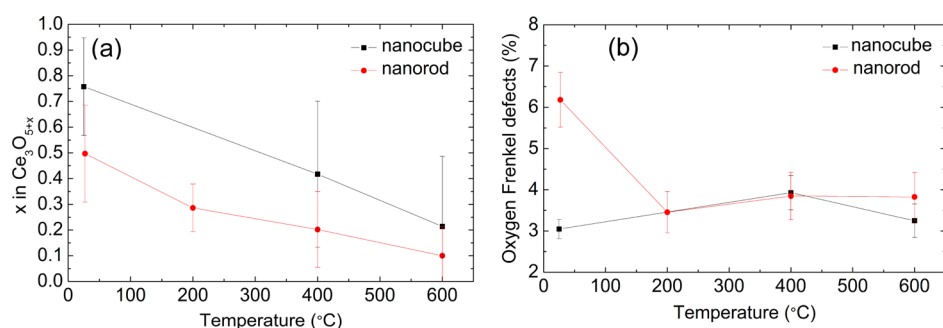


Figure 8. (a) Amount of residual oxygen in the surface oxygen defect phase Ce_3O_{5+x} ($0 < x < 1$, S.G. $Pnn2$) and (b) concentration of bulk oxygen Frenkel defects refined from short-range neutron PDF data (1.5–10 Å) in the pre-reduced ceria nanocube and nanorod.

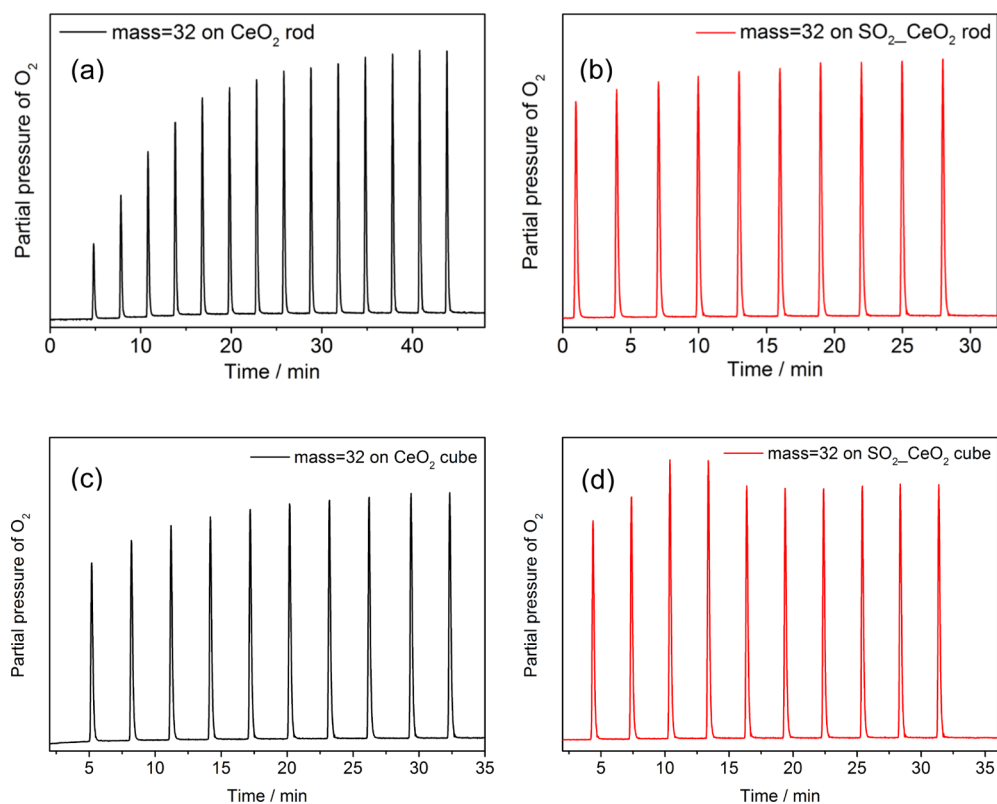


Figure 9. Pulsed O_2 chemisorption on CeO_2 rod (a) and SO_2 treated CeO_2 nanorods (b) after pre-reducing in 4% H_2/Ar at 400 °C for 2 h. Chemisorption on ceria nanocubes and SO_2 -treated ceria are shown in (c) and (d) separately.

observed peak splitting, the drastic particle growth of the nanorod at 600 °C dramatically decreases the surface area and induces surface defect segregation. This has been further confirmed by the formation of new Bragg diffraction peaks (Figure 6) at 600 °C. This particle growth and surface defect segregation will result in the decrease of the overall amounts of surface oxygen-deficient phases, indicating that the optimized operational condition to fully take advantage of the redox properties of the nanorod should be lower than 600 °C.

We further carried out the quantitative analysis of the temperature-dependent data using the two-phase model approach used above. The amounts of oxygen defects in the surface defect phase increase (smaller x values in Ce_3O_{5+x}) for both nanorod and nanocube samples, but with more oxygen vacancies for the nanorod sample relative to the nanocube sample below 400 °C (Figure 8a). For the bulk phase, the concentration of Frenkel-type defects in the nanorod sample is found to decrease from 6.2(7)% at 30 °C to 3.5(5)% at 200 °C

and 3.8(6)% at 400 °C. In contrast, the change in the level of bulk Frenkel defects is relatively small for the nanocube sample at different temperatures (Figure 8b).

3.2. Effect of SO_2/SO_x Exposure on Surface and Bulk Oxygen Defects.

From the pulse chemisorption experiment analysis (Figure 9), the OSC of CeO_2 nanorods was measured to be 91.3 $\mu\text{mol/g}$, a value that is about 3 times that of the nanocubes (36.3 $\mu\text{mol/g}$). These OSC values are in line with what were reported in the literature for ceria samples pre-reduced with H_2 .⁵⁹ While CeO_2 nanocrystals, especially nanorods, show very promising OSC, it is important to test the OSC performance in harsh conditions that are similar to the real operational condition of three-way catalysts. Among them, SO_2 poisoning has been widely recognized as one of the major reasons for performance degradation of CeO_2 nanoparticles. Indeed, the OSC of both samples decreased dramatically upon poisoning, as can be seen in Table 1, and the relative ratios for decreasing are very similar for both

Table 1. Summarized Results on the Quantified OSC from Pulsed O₂ Chemisorption, Structure Defects in Pre-reduced Ceria Nanorod, Nanocube, SO₂-Treated Nanorod, and Nanocube (25 °C)

	nanorod	sulfated nanorod	nanocube	sulfated nanocube
OSC ($\mu\text{mol O}_2/\text{g}$)	91.3	23.5	36.3	9.7
Bulk Frenkel-type defects	0.062(7)	0.043(8)	0.031(3)	0.028(2)
x in surface $\text{Ce}_3\text{O}_{5+x}$	0.52(16)	0.73(12)	0.74(14)	0.82(22)

samples (~75%). To understand the underlying reasons for the dramatic OSC decrease upon SO₂ treatment, especially for the nanorod sample, we carried out temperature-dependent neutron PDF studies of SO₂-treated nanorods and nanocubes. Overall, SO₂ treatment drastically decreases the amounts of oxygen vacancies in the surface defect phases (larger x values in the surface $\text{Ce}_3\text{O}_{5+x}$), as can be seen in Figure 10a,b. In contrast to the pre-reduced nanocrystals, where the oxygen vacancies increase as the temperature increases (red dots in Figure 10), the SO₂-treated ceria nanocrystals maintain nearly constant amounts of oxygen vacancies (black dots in Figure 10) in the surface defect phases at elevated temperatures under vacuum condition. This indicates that the reduction capability of the surface defect phases is drastically inhibited after SO₂ treatment. The SO₂ treatment also decreases slightly the quantity of the bulk oxygen Frenkel defects in both samples, indicating some sulfate/sulfite species progress into the ceria bulk upon 300 °C SO₂ treatment, consistent with a previous spectroscopy study.³⁷ It is worth noting that the overall trend is still distinct between nanorod and nanocube samples: the former shows obvious decrease of the concentration of bulk Frenkel defects as a function of temperature, while the latter shows little change. Taken together, it is likely that the inhibition of the reduction capability of the surface defect

phases of ceria nanocrystals could effectively block the oxygen vacancy transport between the surface/subsurface and the bulk phases. This leads to the slight decrease of oxygen vacancy mobility within bulk ceria, as indicated by the decreased change in oxygen Frenkel defects as a function of temperature in the SO₂-treated nanocrystals (Figures 10c,d).

4. CONCLUSIONS

In summary, this work reveals that the surface oxygen defects in ceria nanocrystals are predominantly the partially reduced $\text{Ce}_3\text{O}_{5+x}$, but with different oxygen vacancy ordering patterns and different amounts of oxygen defect concentration in the nanorods and nanocubes. Ceria nanorods possess much higher concentration of surface oxygen defects relative to the nanocubes, albeit with similar (but slightly higher) concentration of the bulk Frenkel defects. This has been further confirmed by UV Raman study. More interestingly, we observed that with neutron Bragg diffraction, these surface defects in nanorods can crystallize at higher temperatures (e.g., 600 °C) into a long-range oxygen vacancy-ordered defect sublattice. We experimentally confirm the predicted defect formation of partially reduced $\text{Ce}_3\text{O}_{5+x}$ on high energy ceria facets for the first time. The intriguing observation that surface defect phases can take on ordered defect sublattices under certain conditions highlights the needs for further investigation. SO₂ poisoning results in a drastic decrease of OSCs of both ceria nanorods and nanocubes. Structure refinements using neutron PDF indicates that this is rooted in the decrease of surface/subsurface oxygen defects in these nanocrystals, especially under real operating temperatures (i.e., 400 °C). The diminishing of surface/subsurface oxygen defects effectively blocks the oxygen vacancy exchange between the bulk phase and the surface defect phases, resulting in much worse OSC performance of SO₂-treated ceria nanocrystals. This study suggests that tailored surface modification by synthesizing

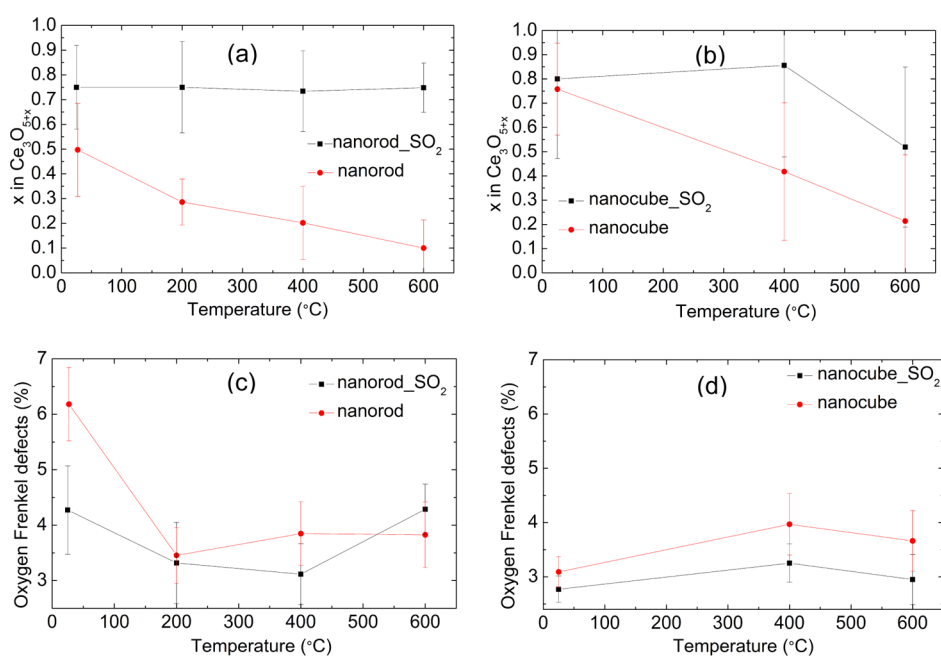


Figure 10. Amount of residual oxygen on the vacancy site in the surface oxygen defect phase $\text{Ce}_3\text{O}_{5+x}$ ($0 < x < 1$, S.G. $Pm\bar{2}$) in the pre-reduced ceria nanorod and SO₂-treated ceria nanorod (a), values for the pre-reduced ceria nanocube and SO₂-treated ceria nanocube (b). Concentration of bulk oxygen Frenkel defects refined from short-range neutron PDF data (1.5–10 Å) in ceria nanorod and SO₂-treated ceria nanorod (c) and in ceria nanocube and SO₂-treated ceria nanocube (d).

nanocrystals with selected exposed facets or chemical modifications that pin key defects at the surfaces are useful strategies to tune the surface defects in ceria nanomaterials. It also highlights the importance of stabilizing surface oxygen defects in CeO₂ to achieve persistent catalytic performance under acid gas environments, such as under the SO₂/SO_x exposure. <http://energy.gov/downloads/doe-public-access-plan>

■ ASSOCIATED CONTENT

SI Supporting Information

The Supporting Information is available free of charge at <https://pubs.acs.org/doi/10.1021/acs.chemmater.1c00156>.

Structure of the fluorite CeO₂; Rietveld refinements of nanorod/nanocube using neutron Bragg diffraction data; Fourier difference map for identifying residual scattering intensities in nanocube/nanorod; long-range oxygen vacancy-ordered structure (Ce₃O_{5+x}) based on {111}, {110}, and {100} facets; local and average structure refinements of nanorod/nanocube using neutron PDF data; PDF data of nanorod and nanocube samples at elevated temperature; UV Raman spectra of pre-reduced CeO₂ nanocube and nanorod; structure refinement results (PDF); and DFT results for formation energies of different oxygen vacancy arrangements in the three plausible bulk Ce₃O₅ phases.

■ AUTHOR INFORMATION

Corresponding Authors

Jue Liu – Neutron Scattering Division, Oak Ridge National Laboratory, Oak Ridge, Tennessee 37831, United States; orcid.org/0000-0002-4453-910X; Email: liuj1@ornl.gov

Zili Wu – Chemical Sciences Division, Oak Ridge National Laboratory, Oak Ridge, Tennessee 37831, United States; orcid.org/0000-0002-4468-3240; Email: wuz1@ornl.gov

Katharine Page – Neutron Scattering Division, Oak Ridge National Laboratory, Oak Ridge, Tennessee 37831, United States; Materials Science and Engineering Department, University of Tennessee, Knoxville, Tennessee 37996, United States; orcid.org/0000-0002-9071-3383; Email: kpage10@utk.edu

Authors

Si Luo – Chemical Sciences Division, Oak Ridge National Laboratory, Oak Ridge, Tennessee 37831, United States

Meijun Li – Chemical Sciences Division, Oak Ridge National Laboratory, Oak Ridge, Tennessee 37831, United States

Victor Fung – Center for Nanophase Materials Sciences, Oak Ridge National Laboratory, Oak Ridge, Tennessee 37831, United States; orcid.org/0000-0002-3347-6983

Bobby G. Sumpter – Center for Nanophase Materials Sciences, Oak Ridge National Laboratory, Oak Ridge, Tennessee 37831, United States; orcid.org/0000-0001-6341-0355

Complete contact information is available at: <https://pubs.acs.org/doi/10.1021/acs.chemmater.1c00156>

Notes

The authors declare no competing financial interest.

■ ACKNOWLEDGMENTS

This work was supported by the Center for Understanding and Control of Acid Gas-Induced Evolution of Materials for Energy (UNCAGE-ME), an Energy Frontier Research Center funded by U.S. Department of Energy, Office of Science, Basic Energy Sciences under award number DE-SC0012577. Part of this work (J.L.) was supported through the U.S. Department of Energy, Office of Science, Office of Basic Energy Sciences, Early Career Research Program award KC040602, under contract number DE-AC05-00OR22725. Part of the work including DFT calculations and the synthesis and OSC test was done at the Center for Nanophase Materials Sciences, which is a DOE Office of Science User Facility operated by Oak Ridge National Laboratory (ORNL). The neutron studies (at NOMAD) used resources at the Spallation Neutron Source, a DOE Office of Science User Facility operated by ORNL.

■ REFERENCES

- (1) Summers, J.; Hegedus, L. L. Effects of platinum and palladium impregnation on the performance and durability of automobile exhaust oxidizing catalysts. *J. Catal.* **1978**, *51*, 185–192.
- (2) Shim, W. G.; Jung, S. C.; Seo, S. G.; Kim, S. C. Evaluation of regeneration of spent three-way catalysts for catalytic oxidation of aromatic hydrocarbons. *Catal. Today* **2011**, *164*, 500–506.
- (3) Li, P.; Chen, X.; Li, Y.; Schwank, J. W. A review on oxygen storage capacity of CeO₂-based materials: Influence factors, measurement techniques, and applications in reactions related to catalytic automotive emissions control. *Catal. Today* **2019**, *327*, 90–115.
- (4) Montini, T.; Melchionna, M.; Monai, M.; Fornasiero, P. Fundamentals and Catalytic Applications of CeO₂-Based Materials. *Chem. Rev.* **2016**, *116*, 5987–6041.
- (5) Deluga, G. A.; Salge, J.; Schmidt, L.; Verykios, X. Renewable hydrogen from ethanol by autothermal reforming. *Science* **2004**, *303*, 993–997.
- (6) Trovarelli, A.; Fornasiero, P. *Catalysis by Ceria and Related Materials*; World Scientific, 2013; Vol. 12.
- (7) Kharton, V. V.; Figueiredo, F. M.; Navarro, L.; Naumovich, E. N.; Kovalevsky, A. V.; Yaremchenko, A. A.; Viskup, A. P.; Carneiro, A.; Marques, F. M. B.; Frade, J. R. Ceria-based materials for solid oxide fuel cells. *J. Mater. Sci.* **2001**, *36*, 1105–1117.
- (8) Liu, X.; Zhou, K.; Wang, L.; Wang, B.; Li, Y. Oxygen vacancy clusters promoting reducibility and activity of ceria nanorods. *J. Am. Chem. Soc.* **2009**, *131*, 3140–3141.
- (9) Duprez, D.; Descorme, C.; Birchem, T.; Rohart, E. Oxygen storage and mobility on model three-way catalysts. *Top. Catal.* **2001**, *16/17*, 49–56.
- (10) Trovarelli, A.; Llorca, J. Ceria catalysts at nanoscale: how do crystal shapes shape catalysis? *ACS Catal.* **2017**, *7*, 4716–4735.
- (11) Harada, K.; Oishi, T.; Hamamoto, S.; Ishihara, T. Lattice oxygen activity in Pr- and La-doped CeO₂ for low-temperature soot oxidation. *J. Phys. Chem. C* **2014**, *118*, 559–568.
- (12) Krishna, K.; Bueno-López, A.; Makkee, M.; Moulijn, J. A. Potential rare earth modified CeO₂ catalysts for soot oxidation: I. Characterisation and catalytic activity with O₂. *Appl. Catal., B* **2007**, *75*, 189–200.
- (13) Mamontov, E.; Egami, T.; Brezny, R.; Koranne, M.; Tyagi, S. Lattice defects and oxygen storage capacity of nanocrystalline ceria and ceria-zirconia. *J. Phys. Chem. B* **2000**, *104*, 11110–11116.
- (14) Ke, J.; Xiao, J.-W.; Zhu, W.; Liu, H.; Si, R.; Zhang, Y.-W.; Yan, C.-H. Dopant-Induced Modification of Active Site Structure and Surface Bonding Mode for High-Performance Nanocatalysts: CO Oxidation on Capping-free (110)-oriented CeO₂:Ln (Ln = La–Lu) Nanowires. *J. Am. Chem. Soc.* **2013**, *135*, 15191–15200.
- (15) Wu, Z.; Li, M.; Howe, J.; Meyer, H. M., III; Overbury, S. H. Probing defect sites on CeO₂ nanocrystals with well-defined surface

- planes by Raman spectroscopy and O₂ adsorption. *Langmuir* **2010**, *26*, 16595–16606.
- (16) He, H.; Dai, H. X.; Au, C. T. Defective structure, oxygen mobility, oxygen storage capacity, and redox properties of RE-based (RE = Ce, Pr) solid solutions. *Catal. Today* **2004**, *90*, 245–254.
- (17) Esch, F.; Fabris, S.; Zhou, L.; Montini, T.; Africh, C.; Fornasiero, P.; Comelli, G.; Rosei, R. Electron localization determines defect formation on ceria substrates. *Science* **2005**, *309*, 752–755.
- (18) Nakajima, A.; Yoshihara, A.; Ishigame, M. Defect-induced Raman spectra in doped CeO₂. *Phys. Rev. B: Condens. Matter Mater. Phys.* **1994**, *50*, 13297.
- (19) Qiu, L.; Liu, F.; Zhao, L.; Ma, Y.; Yao, J. Comparative XPS study of surface reduction for nanocrystalline and microcrystalline ceria powder. *Appl. Surf. Sci.* **2006**, *252*, 4931–4935.
- (20) Reddy, B. M.; Khan, A.; Yamada, Y.; Kobayashi, T.; Loridant, S.; Volta, J.-C. Structural characterization of CeO₂-MO₂ (M = Si⁴⁺, Ti⁴⁺, and Zr⁴⁺) mixed oxides by Raman spectroscopy, X-ray photoelectron spectroscopy, and other techniques. *J. Phys. Chem. B* **2003**, *107*, 11475–11484.
- (21) Mamontov, E.; Egami, T. Structural defects in a nano-scale powder of CeO₂ studied by pulsed neutron diffraction. *J. Phys. Chem. Solids* **2000**, *61*, 1345–1356.
- (22) Murugan, B.; Ramaswamy, A. V. Defect-site promoted surface reorganization in nanocrystalline ceria for the low-temperature activation of ethylbenzene. *J. Am. Chem. Soc.* **2007**, *129*, 3062–3063.
- (23) Binet, C.; Badri, A.; Lavalley, J.-C. A Spectroscopic Characterization of the Reduction of Ceria from Electronic Transitions of Intrinsic Point Defects. *J. Phys. Chem.* **1994**, *98*, 6392–6398.
- (24) Wu, Z.; Li, M.; Overbury, S. H. On the structure dependence of CO oxidation over CeO₂ nanocrystals with well-defined surface planes. *J. Catal.* **2012**, *285*, 61–73.
- (25) Trovarelli, A. Catalytic Properties of Ceria and CeO₂-Containing Materials. *Catal. Rev.* **1996**, *38*, 439–520.
- (26) Zhou, K.; Wang, X.; Sun, X.; Peng, Q.; Li, Y. Enhanced catalytic activity of ceria nanorods from well-defined reactive crystal planes. *J. Catal.* **2005**, *229*, 206–212.
- (27) Mai, H.-X.; Sun, L.-D.; Zhang, Y.-W.; Si, R.; Feng, W.; Zhang, H.-P.; Liu, H.-C.; Yan, C.-H. Shape-selective synthesis and oxygen storage behavior of ceria nanopolyhedra, nanorods, and nanocubes. *J. Phys. Chem. B* **2005**, *109*, 24380–24385.
- (28) Aneggi, E.; Llorca, J.; Boaro, M.; Trovarelli, A. Surface-structure sensitivity of CO oxidation over polycrystalline ceria powders. *J. Catal.* **2005**, *234*, 88–95.
- (29) Qiao, Z.-A.; Wu, Z.; Dai, S. Shape-Controlled Ceria-based Nanostructures for Catalysis Applications. *ChemSusChem* **2013**, *6*, 1821–1833.
- (30) Yan, L.; Yu, R.; Chen, J.; Xing, X. Template-free hydrothermal synthesis of CeO₂ nano-octahedrons and nanorods: investigation of the morphology evolution. *Cryst. Growth Des.* **2008**, *8*, 1474–1477.
- (31) Chen, S.; Xiong, F.; Huang, W. Surface chemistry and catalysis of oxide model catalysts from single crystals to nanocrystals. *Surf. Sci. Rep.* **2019**, *74*, 100471.
- (32) Huang, W.; Gao, Y. Morphology-dependent surface chemistry and catalysis of CeO₂ nanocrystals. *Catal. Sci. Technol.* **2014**, *4*, 3772–3784.
- (33) Ta, N.; Liu, J.; Chenna, S.; Crozier, P. A.; Li, Y.; Chen, A.; Shen, W. Stabilized Gold Nanoparticles on Ceria Nanorods by Strong Interfacial Anchoring. *J. Am. Chem. Soc.* **2012**, *134*, 20585–20588.
- (34) Liu, Y.; Cen, W.; Wu, Z.; Weng, X.; Wang, H. SO₂ poisoning structures and the effects on pure and Mn doped CeO₂: a first principles investigation. *J. Phys. Chem. C* **2012**, *116*, 22930–22937.
- (35) Weng, D.; Li, J.; Wu, X.; Lin, F. Promotional effect of potassium on soot oxidation activity and SO₂-poisoning resistance of Cu/CeO₂ catalyst. *Catal. Commun.* **2008**, *9*, 1898–1901.
- (36) Tumuluri, U.; Rother, G.; Wu, Z. Fundamental Understanding of the Interaction of Acid Gases with CeO₂: From Surface Science to Practical Catalysis. *Ind. Eng. Chem. Res.* **2016**, *55*, 3909–3919.
- (37) Tumuluri, U.; Li, M.; Cook, B. G.; Sumpter, B.; Dai, S.; Wu, Z. Surface Structure Dependence of SO₂ Interaction with Ceria Nanocrystals with Well-Defined Surface Facets. *J. Phys. Chem. C* **2015**, *119*, 28895–28905.
- (38) Liu, H.; Fan, Z.; Sun, C.; Yu, S.; Feng, S.; Chen, W.; Chen, D.; Tang, C.; Gao, F.; Dong, L. Improved activity and significant SO₂ tolerance of samarium modified CeO₂-TiO₂ catalyst for NO selective catalytic reduction with NH₃. *Appl. Catal., B* **2019**, *244*, 671–683.
- (39) Kresse, G.; Furthmüller, J. Efficiency of Ab-Initio Total Energy Calculations for Metals and Semiconductors Using a Plane-Wave Basis Set. *Comput. Mater. Sci.* **1996**, *6*, 15–50.
- (40) Kresse, G.; Furthmüller, J. Efficient iterative schemes for ab initio total-energy calculations using a plane-wave basis set. *Phys. Rev. B: Condens. Matter Mater. Phys.* **1996**, *54*, 11169–11186.
- (41) Perdew, J. P.; Burke, K.; Ernzerhof, M. Generalized Gradient Approximation Made Simple. *Phys. Rev. Lett.* **1996**, *77*, 3865–3868.
- (42) Blöchl, P. E. Projector Augmented-Wave Method. *Phys. Rev. B: Condens. Matter Mater. Phys.* **1994**, *50*, 17953–17979.
- (43) Dudarev, S. L.; Botton, G. A.; Savrasov, S. Y.; Humphreys, C. J.; Sutton, A. P. Electron-Energy-Loss Spectra and the Structural Stability of Nickel Oxide: An LSDA+U Study. *Phys. Rev. B: Condens. Matter Mater. Phys.* **1998**, *57*, 1505–1509.
- (44) Monkhorst, H. J.; Pack, J. D. Special Points for Brillouin-Zone Integrations. *Phys. Rev. B: Condens. Matter Mater. Phys.* **1976**, *13*, 5188–5192.
- (45) Coelho, A. A. TOPAS and TOPAS-Academic: an optimization program integrating computer algebra and crystallographic objects written in C++. *J. Appl. Crystallogr.* **2018**, *51*, 210–218.
- (46) Usher, T.-M.; Olds, D.; Liu, J.; Page, K. A numerical method for deriving shape functions of nanoparticles for pair distribution function refinements. *Acta Crystallogr., Sect. A: Found. Adv.* **2018**, *74*, 322–331.
- (47) Clark, A. H.; Marchbank, H. R.; Hyde, T. I.; Playford, H. Y.; Tucker, M. G.; Sankar, G. Reverse Monte Carlo studies of CeO₂ using neutron and synchrotron radiation techniques. *Phys. Scr.* **2017**, *92*, 034002.
- (48) Farrow, C. L.; Billinge, S. J. L. Relationship between the atomic pair distribution function and small-angle scattering: implications for modeling of nanoparticles. *Acta Crystallogr., Sect. A: Found. Adv.* **2009**, *65*, 232–239.
- (49) Cargill, G. S. Influence of neglected small-angle scattering in radial distribution function analysis. *J. Appl. Crystallogr.* **1971**, *4*, 277–283.
- (50) Liu, J.; Olds, D.; Peng, R.; Yu, L.; Foo, G. S.; Qian, S.; Keum, J.; Guiton, B. S.; Wu, Z.; Page, K. Quantitative analysis of the morphology of {101} and {001} faceted anatase TiO₂ nanocrystals and its implication on photocatalytic activity. *Chem. Mater.* **2017**, *29*, 5591–5604.
- (51) Liu, J.; Yu, L.; Hu, E.; Guiton, B. S.; Yang, X.-Q.; Page, K. Large-Scale Synthesis and Comprehensive Structure Study of δ-MnO₂. *Inorg. Chem.* **2018**, *57*, 6873–6882.
- (52) Murgida, G.; Ferrari, V.; Llois, A. M.; Ganduglia-Pirovano, M. V. Reduced CeO₂ (111) ordered phases as bulk terminations: Introducing the structure of Ce₃O₅. *Phys. Rev. Mater.* **2018**, *2*, 083609.
- (53) Kümmerle, E. A.; Heger, G. The structures of C-Ce₂O_{3+δ}, Ce₇O₁₂, and Ce₁₁O₂₀. *J. Solid State Chem.* **1999**, *147*, 485–500.
- (54) Olbrich, R.; Murgida, G. E.; Ferrari, V.; Barth, C.; Llois, A. M.; Reichling, M.; Ganduglia-Pirovano, M. V. Surface stabilizes ceria in unexpected stoichiometry. *J. Phys. Chem. C* **2017**, *121*, 6844–6851.
- (55) Paier, J.; Penschke, C.; Sauer, J. Oxygen defects and surface chemistry of ceria: quantum chemical studies compared to experiment. *Chem. Rev.* **2013**, *113*, 3949–3985.
- (56) Taniguchi, T.; Watanabe, T.; Sugiyama, N.; Subramani, A. K.; Wagata, H.; Matsushita, N.; Yoshimura, M. Identifying defects in ceria-based nanocrystals by UV resonance Raman spectroscopy. *J. Phys. Chem. C* **2009**, *113*, 19789–19793.
- (57) Gouadec, G.; Colomban, P. Raman Spectroscopy of nanomaterials: How spectra relate to disorder, particle size and mechanical properties. *Prog. Cryst. Growth Char. Mater.* **2007**, *53*, 1–56.
- (58) Désaunay, T.; Bonura, G.; Chiodo, V.; Freni, S.; Couzinié, J.-P.; Bourgon, J.; Ringuedé, A.; Labat, F.; Adamo, C.; Cassir, M. Surface-

dependent oxidation of H₂ on CeO₂ surfaces. *J. Catal.* **2013**, *297*, 193–201.

(59) Zhang, J.; Kumagai, H.; Yamamura, K.; Ohara, S.; Takami, S.; Morikawa, A.; Shinjoh, H.; Kaneko, K.; Adschiri, T.; Suda, A. Extra-Low-Temperature Oxygen Storage Capacity of CeO₂Nanocrystals with Cubic Facets. *Nano Lett.* **2011**, *11*, 361–364.